Electronic Supplementary Information (ESI) for:

Delayed Vibrational Modulation of the Solvated GFP Chromophore into a Conical Intersection

Miles A. Taylor,[†,¶] Liangdong Zhu,[†,‡,¶] Nikita D. Rozanov,[†,§] Kenneth T. Stout,[†,§] Cheng Chen,[†] and Chong Fang*[,†,‡]

[†]Department of Chemistry, Oregon State University, 153 Gilbert Hall, Corvallis, Oregon, 97331-4003, United States

[‡]Department of Physics, Oregon State University, 301 Weniger Hall, Corvallis, Oregon, 97331-6507, United States

[§]School of Chemical, Biological and Environmental Engineering, 116 Johnson Hall, Corvallis, Oregon, 97331-8618, United States

[¶]M.A.T. and L.Z. contributed equally to this work.

*To whom correspondence may be addressed. E-mail: Chong.Fang@oregonstate.edu.

Table of Contents

ESI Text

Further Motivation to Study the GFP Model Chromophore in Solution. In this work, we aim to track the atomic choreography of the green fluorescent protein (GFP) chromophore analogue *p*-HBDI in basic aqueous solution using the newly developed wavelength-tunable femtosecond stimulated Raman spectroscopy (FSRS, see main text). This methodology allows us to provide novel insights into the "dark secrets" of HBDI during its photoinduced isomerization in solution instead of highly efficient radiative emission (e.g., fluorescence) in a protein matrix. Previous ultrafast electronic spectroscopy by Meech, Tonge, van Grondelle, Larsen, et al.[1-3] has revealed the following molecular insights: (1) there exists a conical intersection (CI) that enables efficient radiationless internal conversion from S_1 to S_0, essentially a molecular "funnel" for de-excitation, (2) the radiationless process is not viscosity controlled with large-scale intramolecular reorganization, and (3) the ultrafast internal conversion is an intrinsic property of the chromophore skeleton that could be affected by the local microenvironment including charge distribution or H-bonding. Later, Gepshtein, Huppert and Agmon described active modes leading to facile internal conversion not readily retrievable from the time-resolved fluorescence measurements, and the importance of nonlocal, multi-point twisting motions for the chromophore with an intrinsic conformational distribution that can manifest inhomogeneous kinetics (e.g., excited state decay, conformational relaxation) in solution environment.[4]

In contrast, when inside a protein matrix such as GFP, internal water molecules may provide further H-bonding, stabilization, and structural constraints for the embedded chromophore, restricting the rotational freedom of the distal phenolic ring.[5-7] Despite the internal conversion ($S_1 \rightarrow S_0$) of its protonated chromophore on ~200 ps timescale due to its rotationally symmetrical phenolic C–O bond along the proposed rotational axis[6,8] (i.e., the adjacent bridging C–C bond,

see Figure 1b for the chemical structure of HBDI chromophore), the highly effective excited state proton transfer (ESPT) leads to bright green fluorescence from the lower electronic state corresponding to a deprotonated chromophore. This is an excellent example of ESPT-facilitated radiative emission outpacing radiationless loss channels, and the H-bonding chain connects the phenolic hydroxyl group to internal water molecules and protein residues along the well-defined ESPT chain, which plays a central role in photochemistry of the chromophore.[7,9]

These fundamental and powerful concepts are highly relevant for our current work because FSRS represents a complementary structural dynamics technique[7,9-11] (when compared to the time-resolved IR, for instance)[12-14] that opens new avenues to elucidate actual atomic motions of the GFP model chromophore leading to a CI on ultrafast timescales in aqueous solution. The pre-CI conformational motions could be modeled with an inhomogeneous distribution in close relation to solvation, and rotations of the phenyl ring with a "paddle orientation" as well as the imidazolinone ring both out of plane (OOP) were discussed as possible scenarios.[4] Such OOP motions have become of a focus of our study and the 2D-FSRS target during analysis of the coherent quantum beating signal (see main text, especially Figures 3 and 5). Since we do not directly observe the solvent modes here, a comparison between the chromophore modes in different solvent environments (see main text) can provide further insights into the functional relevance of certain atomic motions during the photoinduced process.[15]

In particular, the impulsively excited vibrational coherence or wavepacket dynamics[7,16,17] could manifest as quantum beats during the temporal evolution of individual Raman modes following fs photoexcitation (*vide infra*, e.g., Figures S6, S8, and S9).[7,9,11,15,17,18] Since the internal conversion is expected to occur most efficiently where the excited and ground state surfaces approach or cross (e.g., via a CI, where the Born-Oppenheimer approximation breaks

down), the chromophore intramolecular twisting motions seem to play an important role in the electronically excited state. In other words, an effective CI usually involves a large vibronic coupling between electronic states (e.g., S_1 and S_0) hence supporting an ultrafast crossing process.[19-21] That way we can elucidate the interplay among the rupture of ground-state extended conjugation upon electronic excitation, intramolecular charge transfer, and ring twisting motions, thus providing a fundamental understanding of the photoinduced reactions of ring-conjugated molecular systems, also leading to future design of molecular machines with new functions. This mechanism coupled with recent engineering effort[9,22-24] is particularly relevant due to the continuing and burgeoning interest of GFP fluorescence from an interdisciplinary context from molecular spectroscopy, physical chemistry, bioorganic chemistry, biophysics, bioimaging, bioengineering, nanophotonics to optogenetics.

Solvent Dependence of Mode Frequencies Aids Vibrational Assignment. The isolated chromophore in solution is not really "isolated" *per se*, and the Raman spectrum contains detailed information about vibrational motions. The spectral shift of vibrational bands in different solvents is a clear indication that the chromophore is not only surrounded by solvent molecules, but also forming specific hydrogen bonds with them. Based on a series of ground-state FSRS measurements previously performed at UC Berkeley with an 800 nm Raman pump,[7] the phenolic C─O stretch frequency of the neutral HBDI chromophore is 1230 and 1228 cm^{-1} in CH_3OH and CH_3CN, respectively. This mode blue shifts to 1241 and 1242 cm^{-1} for the anionic chromophore in CH_3OH and CH_3CN (both with 5% (v/v) 1 M NaOH), respectively, indicating the departure of the phenolic proton and increase of the phenolic C─O double-bond character. Upon 400 nm photoexcitation, the 1241 cm^{-1} mode blue shifts to 1264 cm^{-1} within the cross-

correlation time of ~130 fs,[7] and the excited state mode intensity decays biexponentially with time constants of ~290 fs (89%) and 1 ps (11%). The difference between the longer time constant of 1 ps (herein) and 2.9 ps (Table S2) arises from the variation in solvents (methanol *vs.* water) and the Raman pump wavelengths (794 nm vs. 550 nm) being used. Further comparisons can be made between water and the water-glycerol solution, because the latter environment should effectively lengthen the conformational transition from the initially excited coplanar chromophore to a twisted one. Modest effect on the observed structural dynamics may infer some volume-conserving twisting motions.[1,4] Nevertheless, the overall trend corroborates the photoinduced ultrafast isomerization of the anionic HBDI chromophore in solution.

Due to a similar electron redistribution as the chromophore protonation state changes, the observed imidazolinone ring C=N stretching with some exocyclic C=C stretching motion at 1568 and 1567 cm^{-1} of the neutral chromophore redshifts to 1558 and 1557 cm^{-1} of the anionic chromophore in CH_3OH and CH_3CN, respectively.

The higher-frequency mode in association with the bridge C=C and phenol ring C=C stretching motions at 1645 and 1650 cm^{-1} of the neutral chromophore redshifts to 1634 and 1635 cm^{-1} of the anionic chromophore in CH_3OH and CH_3CN, respectively. In particular, the observed lower mode frequency (i.e., 1645<1650, 1634<1635) is in accord with a larger quantum "box" due to more effective H-bonding in methanol than that in acetonitrile. These solvent-dependent Raman mode frequencies provide additional support for the vibrational assignment listed below for the anionic HBDI chromophore in water (see Figure S2).

ESI Figures

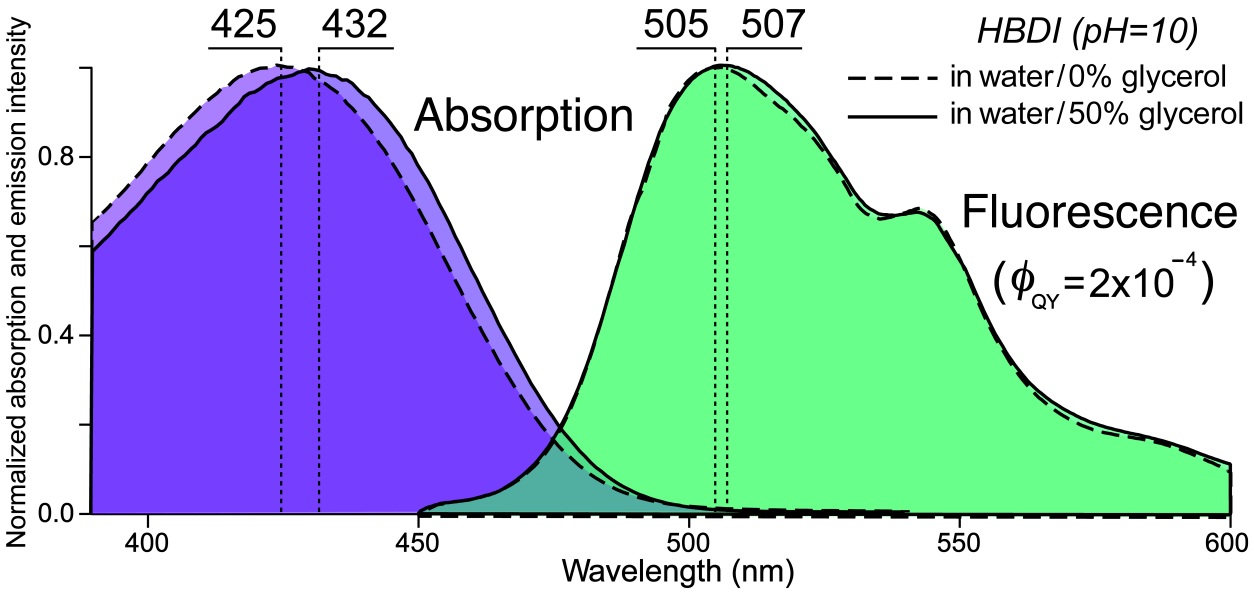

Figure S1. Steady-state absorption (violet shades) and fluorescence (green shades) spectroscopy of HBDI in basic aqueous solution (pH=10) as a GFP model chromophore. The spectrum with additional 0% and 50% glycerol is shown by the dashed and solid curves, respectively. The spectra are all normalized for comparison. The peak positions are labeled by vertical dotted lines.

The minuscule fluorescence quantum yield (FQY, $\Phi=2.1\times10^{-4}$) indicates that the HBDI chromophore is essentially non-fluorescent in water at room temperature.[1,3,25] The absorption and emission line shapes (e.g., width, asymmetry, temperature dependence) have been discussed in literature[4,26] which are not the focus of this work, yet some related discussions can be found below and in main text.

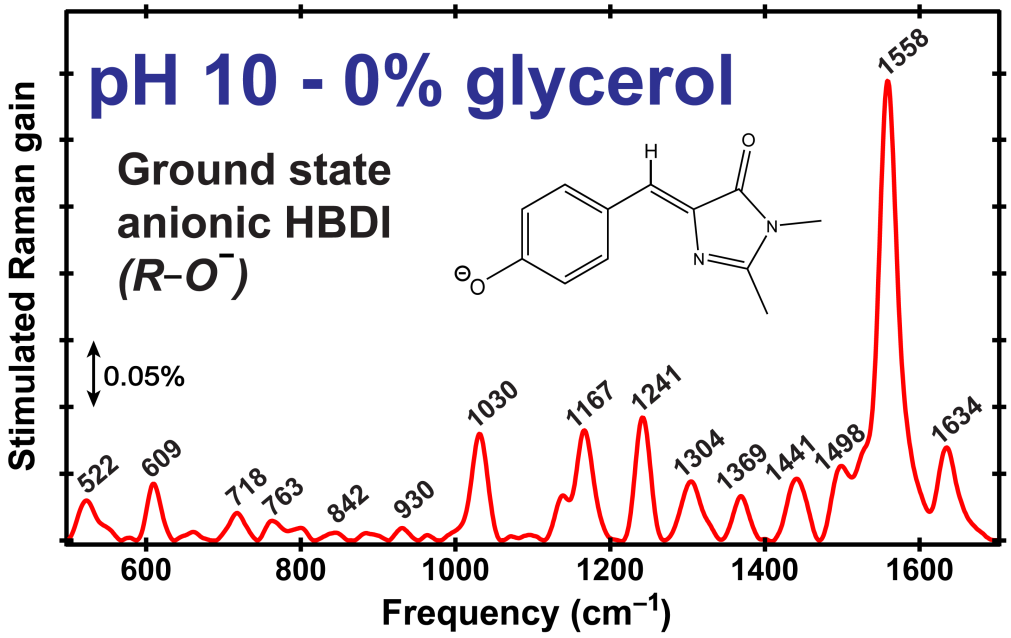

Ground state frequency (cm^{-1})	Calculated DFT frequency (cm^{-1})	Vibrational mode assignment (major)
522	516	Phenolate ring symmetric HOOP, bridge-HOOP, imid. ring OOP deform
609	623	Phenolate ring with weak imidazolinone ring i.p. deformation
718	712	Imidazolinone ring i.p. deformation and bridge CCC bending
763	755	Imidazolinone and phenolate ring i.p. breathing
842	839	Phenolate ring symmetric HOOP and weak bridge-HOOP
930	923	Imidazolinone ring i.p. deformation
1030	1028	Imidazolinone ring i.p. deformation and methyl bending motions
1167	1181	Imidazolinone ring i.p. deformation, phenolate ring C–H bending
1241	1253	Phenolate and bridge C–H rocking, phenolate ring i.p. deformation
1304	1301	Phenolate ring and bridge C–H rocking, and imid. ring i.p. deformation
1369	1374	Imidazolinone ring i.p. deformation, bridge and phenolate C–H rocking
1441	1468	Phenolate ring C=C stretching with bridge CCC stretching
1498	1496	Phenolate ring asymmetric C=C stretch and ring C–H rocking
1558	1554	Imidazolinone C=N and bridge C=C stretch (delocalized)
1634	1631	Phenolate ring C=C (w/ bridge C=C) and imid. ring C=O stretch

i.p., in-plane; HOOP, hydrogen out-of-plane motion; imid., imidazolinone. Scaling factor = 0.985

Figure S2. Ground state FSRS spectrum of the anionic HBDI in aqueous solution (pH=10). Raman mode assignment is aided by quantum chemistry density functional theory (DFT) calculations in Gaussian 09,[27] at the RB3LYP exchange-correlation functional level with basis sets 6-31G+(d,p) and the IEFPCM (Polarizable Continuum Model using Integral Equation Formalism variant, solvent = water). The calculated frequency scaling factor is 0.985.[28,29]

In order to elucidate key structural motions leading to a conical intersection on ultrafast timescales, we need to study a system with an ideally unidirectional reaction coordinate, without major competing pathways. For the GFP model chromophore in aqueous solution, we tune the pH to 10 which is ~2 units above the pK_a at the phenolic hydroxyl site[30-32] so the anionic chromophore is the predominant species. In addition to the resultant absence of excited state proton transfer (ESPT), the higher sensitivity of the anionic chromophore (than the neutral chromophore) to surrounding solvent molecules arises from solvent stabilization of the negative charge on the phenolic oxygen.[33-35] We also observed a consistent 10–20 cm^{-1} mode frequency redshift of the bands above 1550 cm^{-1} in the anionic form when compared to the neutral form.[31]

Notably, these vibrational marker bands show a similar pattern for the HBDI chromophore in solution and protein environment,[31] indicating that the pre-resonance Raman enhancement is mainly applicable for the light-absorbing chromophore not the surrounding protein residues. The protein matrix confinement effect is especially pronounced on low-frequency vibrational modes of the embedded chromophore. One would imagine that whether the chromophore is attached to protein backbone or not, the autocyclic three-residue serine-tyrosine-glycine (SYG, see Figure 1a) chromophore should contain many similar vibrational modes across the conjugated two-ring structure. However, within the protein at thermal equilibrium and electronic ground state, the chromophore is effectively locked into a *cis* conformation due to limited flexibility from the surrounding H-bonding network and protein residues, which could suppress the intensity of the out-of-plane (OOP) modes but not so much for the in-plane modes. This notable difference in local environment presents itself in the Raman spectrum of HBDI in solution below ~1000 cm^{-1}: the lower frequency OOP modes exhibit relatively stronger intensity than the higher frequency in-plane vibrational modes. Inside the protein pocket, such a trend is largely reversed.[8,36]

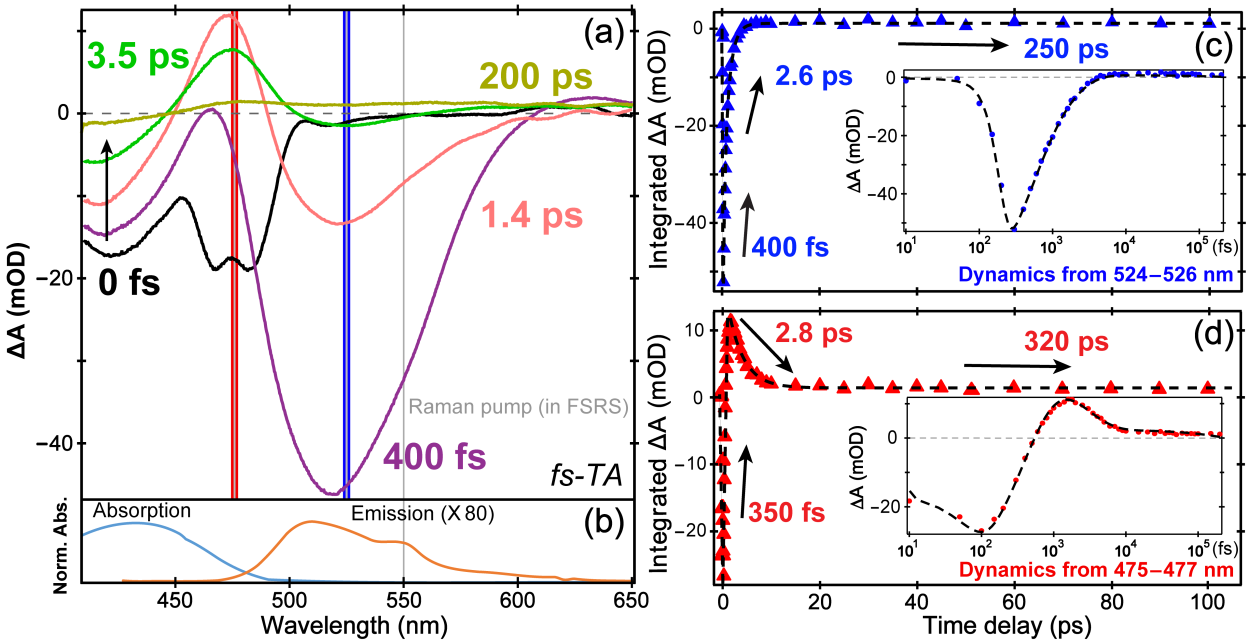

Figure S3. Steady-state and time-resolved electronic spectroscopy of the GFP model chromophore in solution. (a) Transient absorption of anionic HBDI in pH=10 aqueous solution after 400 nm photoexcitation. Representative spectra at time delay of 0 fs, 400 fs, 1.4 ps, 3.5 ps, and 200 ps are shown in black, violet, orange red, green, and brown yellow traces, respectively. Characteristic regions for spectral signal integration and dynamic plot are highlighted by blue and red rectangular boxes which correspond to (c) and (d), respectively. (b) Steady-state UV/Visible absorption (cyan) and spontaneous emission spectrum with 390 nm excitation (orange). The latter spectrum from the essentially non-fluorescent HBDI in water at room temperature is multiplied by ~80 at this experimental condition to compare with the former spectrum. (c) Integrated plot of the dominant stimulated emission signal from 524—526 nm at time delay points of 0—100 ps after 400 nm photoexcitation. The least-squares fit in dashed line (black) is overlaid with data points (blue) and the associated time constants are noted by the arrows. The semi-logarithmic plot is shown in the inset to highlight the early-time dynamics. (d) The integrated plot of the dominant excited state absorption signal from 475—477 nm at time

delay points of 0—100 ps after 400 nm photoexcitation. With the same format as (c), the least-squares fit in dashed line (black) is overlaid with data points (red triangles) in main plot and with early-time data points (red circles) in the inset, respectively.

The small fluorescence shoulder peak at ~550 nm in Figure S3b may indicate an additional radiative emission pathway from the chromophore in the electronic excited state, which was less resolved in a previous study on the fluorescence peak shape of the anionic *p*-HBDI chromophore from 122–298 K.[26] The subtle difference from an inhomogeneously broadened fluorescence spectrum requires further investigation, which is underway in our lab to provide more details about the electronic excited state potential energy surface (PES) of anionic HBDI in aqueous solution. The existence of an intermediate electronic state with charge-separated character is corroborated by the broadness of the SE band at early times[24] (Figure S3a) with the transient ESA band dynamics shown in Figure S3d, which could involve characteristic nuclear motions of solute molecules surrounded by the highly labile solvent molecules (water in the current work).

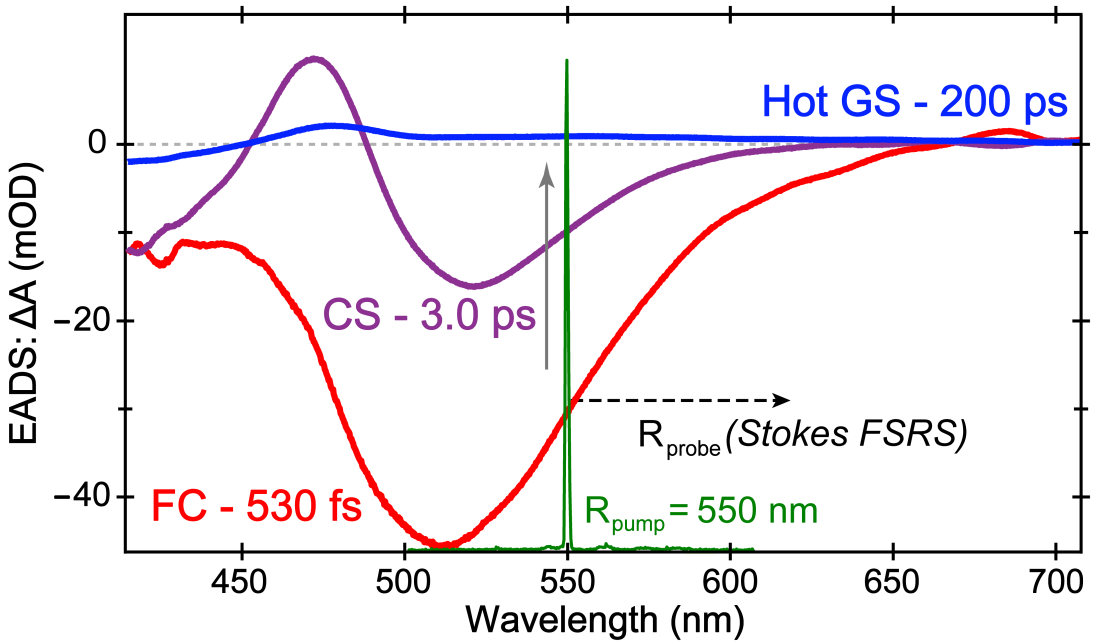

Figure S4. Global analysis of the anionic HBDI chromophore in aqueous solution (pH=10). The sequential three-component model yields the evolution-associated difference spectra (EADS) from a Franck-Condon (FC, 530 fs lifetime, red) state, an intermediate charge-separated (CS, 3.0 ps lifetime, violet) state to an unrelaxed ground state (hot GS, 200 ps lifetime, blue). Time evolution is indicated by the gray upward arrow. The Raman pump at 550 nm (green) and Raman probe to the red side in the Stokes FSRS experiment are also depicted in the figure. Notably, the Raman pump is close to the stimulated emission (SE) band intensity maximum.

The assignment of the third component to hot GS (not a trapped, non-radiative excited state) is aided by the excited state FSRS data in Figure 2. Notably, the spectral "gap" after ~6 ps with no clearly discernible Raman peaks indicates that the molecule passes through a CI and returns to GS likely still in a two-ring twisted conformation. The significantly altered resonance Raman conditions therein lead to much reduced Raman peak intensities even though the hot GS still differs from the original equilibrated GS in both the electronic and vibrational domains.

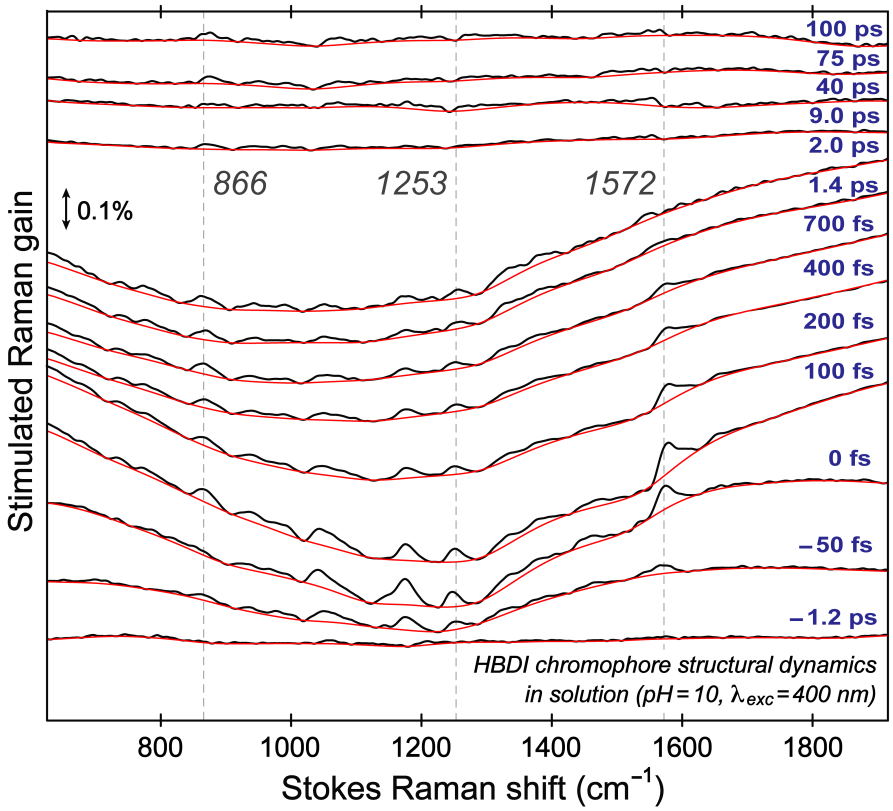

Figure S5. Semi-automatic baselines of the time-resolved FSRS using an asymmetric least-squares algorithm in R software (for statistical computing and graphics). The experimental raw data traces of photoexcited HBDI chromophore in aqueous solution (pH=10) at representative time delay points are shown in black and the baselines in red. The stimulated Raman gain magnitude of 0.1% is depicted by the vertical double-arrowed line. Three excited-state (ES) maker bands discussed in the main text are labeled and highlighted by the gray dashed lines.

Notably due to the pre-resonantly enhanced Raman peaks by the 550 nm Raman pump (close to the SE band max), the spline baselines semi-automatically drawn or manually drawn yield no appreciable differences for the ES Raman peaks and the ensuing spectral data analysis. At early times when the ES-FSRS signal is the strongest, the spectral dip due to the ground-state bleach (off-resonance) is very small in comparison. Therefore, the GS addback is not necessary at early times or it introduces minimal impact to the excited-state peak analysis (e.g., Figure 2, Table 1).

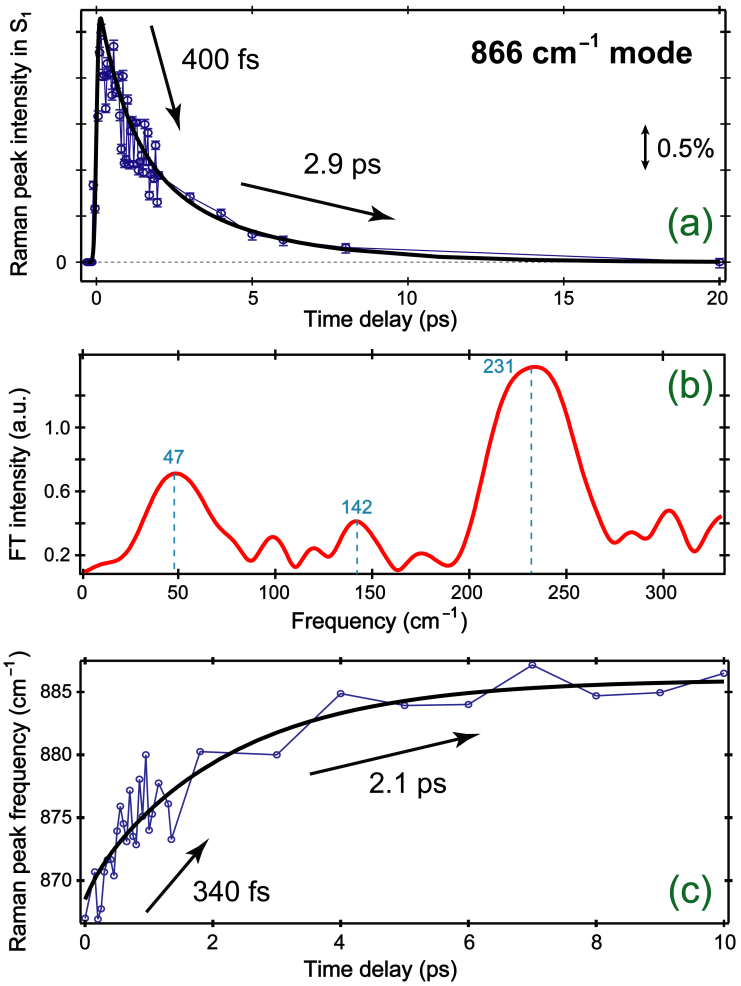

Figure S6. Early-time dynamics of the 866 cm^{-1} mode in the electronic excited state of anionic HBDI in pH=10 aqueous solution. (a) Integrated peak intensity plot of the specific Raman band of interest up to 20 ps after 400 nm photoexcitation. Coherent quantum beating is apparent, which corresponds to the oscillatory component on top of the incoherent biexponential fit (black curve, time constants noted). (b) FT intensity plot of the oscillations reveals three modulating modes at ~231, 47, and 142 cm^{-1} in the order of decreasing prominence (see Figure 5a for their time dependence). (c) Peak frequency plot up to 10 ps following photoexcitation with the least-squares biexponential fit (time constants noted). Some oscillations are present from 0–2 ps but less obvious than the intensity oscillations in (a), which may be due to the broad peak width in the excited state and the resultant uncertainty of determining the peak center frequency.

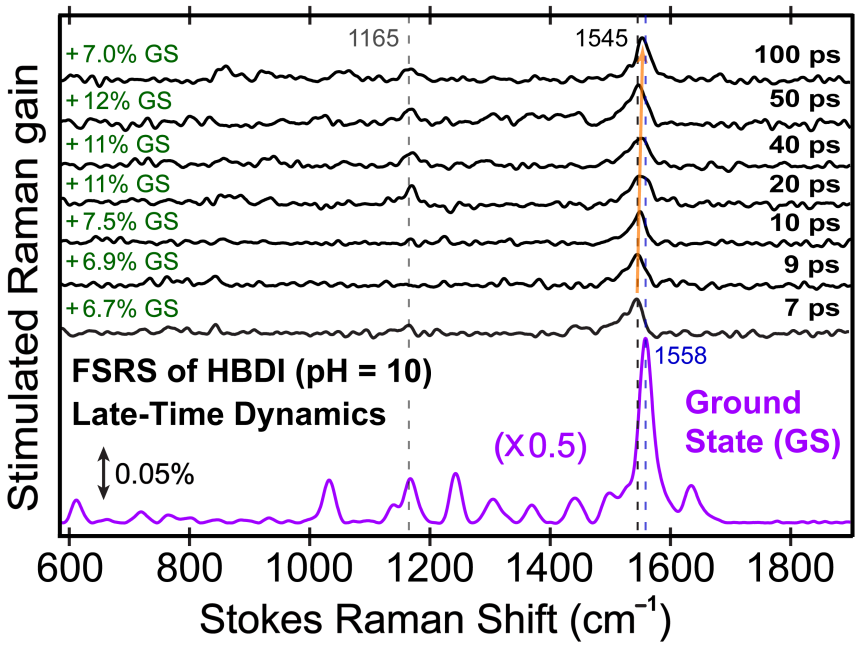

Figure S7. Representative late-time FSRS spectra of anionic HBDI in pH=10 aqueous solution after ground state (GS) addback. Prominent Raman peaks are labeled by vertical dashed lines, which represent a redshift from the corresponding peaks in the original ground state (violet, scaled and plotted for comparison). The addback ratio of the ground state spectrum is denoted in green on the left side by each transient spectral trace up to 100 ps after 400 nm photoexcitation. The orange arrow highlights the gradual blueshift of the transient Raman peak at ~1545 cm^{-1} toward the "cold" ground state peak frequency at 1558 cm^{-1} (blue) on the tens of ps timescale.

The broader peak widths from 7—100 ps time delay corroborates the hot ground state (HGS) nature of the pertinent molecular species, and the ~1545 cm^{-1} peak closely matches the 1542 cm^{-1} red-shifted ES peak in Figure 2a before the twisted chromophore crosses the S_1/S_0 CI (i.e., the spectrally silent region).[19,37] The vibrational linewidth of the observed modes provides a qualitative assignment of ground or excited state features. Since the excited-state lifetime of the model GFP chromophore in solution is typically on the sub-ps to ps regime (Table S2) while the lifetime of ground-state peaks is much longer (consistent with Figures S4 and S7),[11,38] the wider

peaks in the excited state spectra (Figure 2) are in accord with the Heisenberg uncertainly principle (i.e., $\Delta E \cdot \Delta t \geq \hbar/2$). Further relaxation in the electronic ground state may experience changed resonance conditions with the 550 nm Raman pump, reflected by the initial increase and later decrease of the GS addback ratios. Notably, in a typical FSRS experiment with the laser pulse conditions we used, less than 15% of the sample molecules will be photoexcited.[7,9,11] In general, the addback ratios in Figure S7 at later times after the system passes through the S_1/S_0 CI should decrease because more original ground state species are recovered on that timescale. The complication arises from the overlap between the ~1545 cm^{-1} HGS peak and the 1542 cm^{-1} excited state (ES) peak around the TICT and CI regions (<5 ps), and the change of resonance conditions as the HGS species evolve in S_0. As ES peaks diminish on the few ps timescale due to the TICT formation and a rapid S_1/S_0 CI crossing, the nascent HGS species experience better resonance enhancement with the 550 nm Raman pump than the "cold" GS species, so the apparent GS dip is smaller than what it should be (e.g., at ~7 ps). As the HGS species relax into the lower portion of S_0 PES (Figure 6) and the resonance condition worsens, the GS dip seems larger, hence the observed addback ratio increase (e.g., from 7 to 50 ps). On the hundreds of ps timescale (~250 ps in Figure 6), the ground-state isomerization recovers more original S_0 species while the resonance condition remains largely unchanged, hence the addback ratio decrease (e.g., from 50 to 100 ps).[1,11] In addition, these late-time spectra were convoluted with some residual signal from the not fully recovered HBDI chromophore likely trapped in a still-twisted geometry.

The observed Raman peak blueshift and narrowing at late times is consistent with vibrational cooling and repopulation of the original GS which involves a twist back to the two-ring planarity. A closer look of such processes is expected to benefit from better resonance of the more relaxed ground-state chromophore vibrational motions with a bluer Raman pump (see Figure S3).[9]

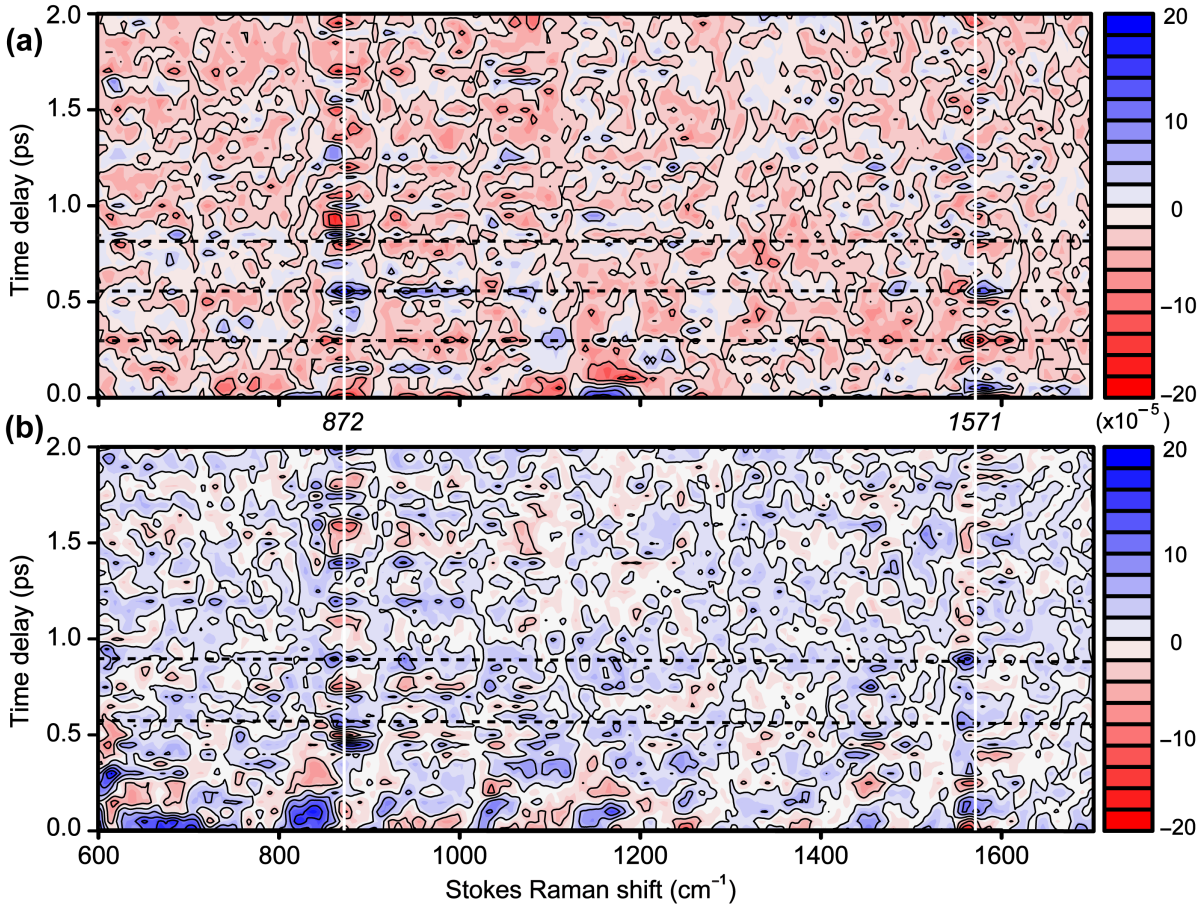

Figure S8. Coherent residuals of time-resolved FSRS spectra after subtracting the incoherent intensity decay component from global analysis in Glotaran for the anionic HBDI chromophore (a) without and (b) with 50% (v/v) glycerol in pH=10 aqueous solution. The time window is displayed up to 2 ps after 400 nm photoexcitation, and the spectral window spans more than 1100 cm^{-1} (see the experimental data in Figure 2). The horizontal black lines show that the prominent intensity oscillations are largely in phase between the two probing Raman modes at ~872 and 1571 cm^{-1}, the frequency locations of which are highlighted by the vertical white lines.

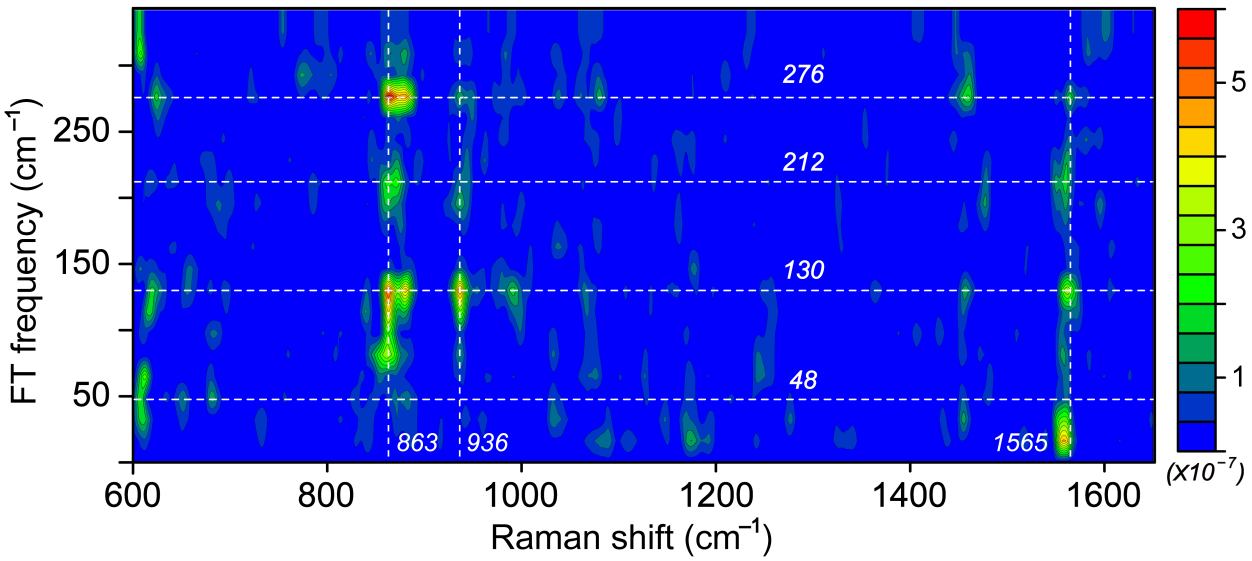

Figure S9. 2D-FSRS of the HBDI anion in the 50% (v/v) glycerol-water mixture uncovers prominent vibrational coupling between Raman marker bands up to 2 ps after 400 nm photoexcitation. The white dashed lines highlight the peak frequencies along the Raman shift axis (probing/coupling modes) as well as the FT frequency axis (modulating/tuning modes).

The probing marker bands at ~863, 936, and 1565 cm^{-1} represent a redshift from their counterparts in the 2D-FSRS spectrum of the HBDI anion in aqueous solution without glycerol (see Figure 3). The modulating low-frequency modes also differ with the addition of 50% (v/v) glycerol in that the ~276, 130, 212, and 48 cm^{-1} modes become prominent in the order of decreasing intensity. In particular, the 276 cm^{-1} mode is not present without glycerol, while the 130 and 212 cm^{-1} modes represent a redshift from the 143 and 227 cm^{-1} modes in aqueous solution without glycerol. These comparative results indicate that local environment affects the solvated chromophore in a way that the photoinduced reaction coordinate (charge transfer and ring twisting in this case) changes on ultrafast timescales. The vibrational frequency redshift for both the tuning and probing modes likely arises from the increased viscosity and more restrictive H-bonding network in the 50% (v/v) glycerol-water mixture. In other words, because we study

the sample system in an identical experimental setup only with 50% (v/v) glycerol added in water, the retardation of characteristic atomic motions (see Table S2 below) and variation of the vibrational anharmonic coupling matrix (as shown in Figure 3 *versus* Figure S9 above) can yield deeper structural dynamics insights into which reaction phase involves the volume-conserving or volume-changing motions. Such nuclear (vibrational) motions could play a functional role in the photoinduced isomerization of the anionic HBDI chromophore (see main text).

ESI Tables

Table S1. Transient absorption peak intensity dynamics of the anionic HBDI in water

Fs-TA feature [a]	Ground state bleaching (GSB) [b]	Excited state absorption (ESA) [c]	Stimulated emission (SE)
Probe wavelength	415 nm	473 nm	520 nm
With 0% glycerol	200 fs (63%) **2.5 ps** (31%) 200 ps (6%)	350 fs (73%) **2.8 ps** (23%) 320 ps (4%)	400 fs (74%) **2.6 ps** (21%) 250 ps (5%)
With 50% glycerol	200 fs (60%) **3.2 ps** (34%) 250 ps (6%)	500 fs (78%) **4.7 ps** (18%) 344 ps (4%)	500 fs (70%) **4.4 ps** (27%) 315 ps (3%)

[a] The representative fs-TA spectra are plotted in Figure S3a. The single wavelength for kinetic analysis is selected near the peak of each broad transient electronic band.

[b] Dynamics of the GSB band below 430 nm represent how fast the molecular population returns to S_0. In principle, the GSB decay time constants provide further corroboration for the "closed-loop" system of HBDI via photoexcitation, twisting, passing through CI, hot ground state relaxation, and original ground state recovery. The >200 ps component represents the major back-twisting motion to the *cis* conformer as the ground state PES provides a strong restoring force (see Figure S7 for the pertinent FSRS data, and Figure 6 for the PES schematic).[31,39,40]

[c] This ESA band overlaps with the shorter wavelength GSB band and the longer wavelength SE band on the fs to ps timescales. The transient nature of this ESA band is corroborated by the second EADS from global analysis of the fs-TA data (Figure S4), which serves as a signature for the intermediate CS state as discussed in main text.

Table S2. Excited state vibrational mode assignment and associated intensity dynamics time constants from the time-resolved FSRS of the anionic HBDI in water

Mode frequency (cm^{-1})		**Calculated mode freq. (cm^{-1})** [b]	**Time constants** [c]		**Vibrational mode assignment (major)**
+ 0% glycerol [a]	**+ 50% glycerol** [a]		**+ 0% glycerol**	**+ 50% glycerol**	
227	N/A	248	N/A	N/A	Global ring out-of-plane (OOP) deformation and bridge CCC OOP bending [d]
618	618	631	250 fs (69%) 1.9 ps (31%)	300 fs (64%) 3.2 ps (36%)	Phenolate ring in-plane deformation and bridge CCC in-plane bending
730	727	734	250 fs (59%) 2.3 ps (41%)	350 fs (57%) 3.1 ps (43%)	Phenolate OOP and bridge OOP motions with HOOP, and imidazolinone OOP deformation
772	773	771	250 fs (62%) 2.2 ps (38%)	350 fs (63%) 3.4 ps (37%)	Bridge HOOP and anti-symmetric phenolate ring HOOP, small-scale imidazolinone OOP deform
866	861	852	400 fs (50%) 2.9 ps (50%)	450 fs (53%) 3.6 ps (47%)	Symmetric phenolate ring HOOP, weak bridge HOOP motion
1045	1045	1073	350 fs (79%) 2.2 ps (21%)	350 fs (80%) 2.9 ps (20%)	Phenolate ring-H scissoring and bridge C–H rocking
1253	1252	1253	300 fs (51%) 2.9 ps (49%)	350 fs (58%) 3.6 ps (42%)	Imidazolinone ring in-plane deformation, phenolate ring-H rocking and bridge C–C stretch

1572	1567	1561	200 fs (74%) 2.0 ps (26%)	240 fs (80%) 3.0 ps (20%)	Phenolate C=C and C=O stretch with bridge CC stretch, imidazolinone C=O [e] and small-scale C=N stretch

[a] The experimental Raman mode center frequency is obtained by least-squares fitting the ground-state FSRS peaks of anionic HBDI in aqueous solution (pH=10) with 0% or 50% glycerol. Three independent data sets on different days were used to obtain the average value and the precision is within 1 cm^{-1}. The Raman pump center wavelength was tuned to 550 nm.

[b] Singlet excited state (S_1) vibrational frequencies of the geometrically optimized anionic HBDI chromophore (see Figure 1b in main text for the chemical structure) are calculated using the time-dependent DFT (TD-DFT) method with RB3LYP theory level and 6-311G+(d,p) basis sets and –1 charge in Gaussian 09.[27] The water solvent effect is incorporated using the integral equation formalism variant polarizable continuum model (IEF-PCM) method. The normal mode frequency scaling factor is 0.97 for the high-frequency modes (>1000 cm^{-1}) and 1.01 for the low-frequency modes (<1000 cm^{-1}) as recommended to account for the frequency-dependent thermal contributions to enthalpy and entropy.[29] The observed Raman modes in Stokes FSRS (Figure 2a and b, main text) is from the anionic HBDI chromophore in S_1 after 400 nm photoexcitation.

[c] Typically, the integrated Raman peak intensities in Figure 2 can be least-squares fitted by two exponentials that capture the essence of early-time structural dynamics of the chromophore. Since the TA spectra reflect the population dynamics of HBDI, we use those time constants in Table S1 as an initial guide for interpreting FSRS dynamics. However, some differences are expected due to the separate tracking of electronic dynamics in TA whereas vibrational dynamics in FSRS. The small increase of the second time constant upon adding 50% (v/v) glycerol is in accord with the reported weak dependence of chromophore modes on medium viscosity.[2,41]

[d] This motion is consistent with the overall volume-conserving picture[3,41] as nearby atoms move in opposite directions out of the chromophore two-ring plane (Figure 4a).

[e] This assignment is corroborated by a transient IR spectroscopic study of the C=O vibration of anionic HBDI in the S_1 state,[40] which did not observe the mode at a similar frequency region above 1680 cm^{-1} for the neutral and cationic HBDI. The C=O mode likely downshifts its frequency to mix with the aromatic ring vibrations as shown in the current mode assignment, consistent with the mesomeric charge delocalization across the conjugated ring system of the photoexcited anionic HBDI chromophore in solution. Notably, using the same level of theory (DFT-RB3LYP) and basis sets (6-311G+(d,p)), this vibrational mode at the electronic ground state (S_0) has the frequency of 1647.3 cm^{-1} which after a frequency scaling of 0.985 yields ~1623 cm^{-1}. The photoinduced mode frequency redshift due to electron redistribution from $S_0 \rightarrow S_1$ is thus apparent from calculations (i.e., 1623$\rightarrow$1561 cm^{-1}).[7,9,13]

Table S3. Frequency shift trend of three Raman marker bands and other key properties as a function of the chromophore ring twisting dihedral angle θ

Mode freq. (cm^{-1}) / Dihedral angle θ (°) [b]	866 [a]	1253 [a]	1572 [a]	Polarizability (a.u.)	Overall energy (a.u.)
– 90	872	1258	1580	383.45	−724.00102307
– 80	881	1256	1588	299.92	−723.99511733
– 60	870	1255	1577	378.37	−724.01302911
– 40	850	1264	1575	360.23	−724.03522701
– 20	852	1270	1576	346.11	−724.05250946
0	852 [c]	1272 [c]	1578 [c]	337.41 [c]	−724.06409524 [c]
20	851	1273	1577	339.45	−724.06184931
40	852	1276	1576	344.58	−724.05488068
60	853	1278	1576	353.66	−724.04304504
80	856	1279	1580	366.30	−724.02721848
90	857	1282	1579	373.44	−724.01828613

[a] The experimentally observed excited state Raman mode frequencies that show charateristic shifts in Figure 2a for the anionic HBDI in water (pH=10), also see Table 1 in main text. The listed normal mode frequencies (unscaled) in this table are from DFT calculations of the geometrically optimized deprotonated chromophore (–1 charge) at the RB3LYP level with 6-31G+(d,p) basis sets and the IEFPCM solvent=water using Gaussian 09 software. To reduce computational costs, the frequency shift trend (not the exact values) in S_0 is used to gain insights into the observed mode frequency shift in S_1 along the particular dihedral twisting coordinate.

[b] This dihedral angle between the bridge C atom and the imidazolinone ring (depicted in Figure 1b) is fixed at discrete values from the positive to negative during DFT calculations to enable the inspection of the chromophore ring-twisting-angle-dependent vibrational mode frequency shifts.

[c] In comparison to these values calculated at $\theta = 0°$ (angle fixed in this table, see Figure 1b for depiction) which correspond to the optimized ground state structure of a nearly planar chromophore in solution,[4,41,42] the unscaled Raman mode frequency blue (red) shift, and the overall energy and electric polarizability increase (decrease) are shown in blue (red) cells. The observed vibrational frequency shifts better match the calculations in the positive θ direction. To further evaluate the robustness of this approach, we also performed the DFT-RB3LYP 6-311G+(d,p) calculations. After geometrical optimization at the electroic ground state, the above-mentioned dihedral angle is essentially zero (i.e., –0.004°) and the unscaled vibrational normal mode frequencies are 854.4, 1276.3, and 1568.4 cm^{-1} with an overall energy of –724.21639540 a.u. The associated vibrational motions are mainly the phenolate ring symmetric HOOP, the phenolate ring H-rock with bridge H-rock, and the phenolate C=C stretch with ring CC stretch and some imidazolinone C=N stretch, respectively.

ESI References

1 N. M. Webber, K. L. Litvinenko and S. R. Meech, *J. Phys. Chem. B*, 2001, **105**, 8036-8039.

2 K. L. Litvinenko, N. M. Webber and S. R. Meech, *J. Phys. Chem. A*, 2003, **107**, 2616-2623.

3 M. Vengris, I. H. M. van Stokkum, X. He, A. F. Bell, P. J. Tonge, R. van Grondelle and D. S. Larsen, *J. Phys. Chem. A*, 2004, **108**, 4587-4598.

4 R. Gepshtein, D. Huppert and N. Agmon, *J. Phys. Chem. B*, 2006, **110**, 4434-4442.

5 K. Brejc, T. K. Sixma, P. A. Kitts, S. R. Kain, R. Y. Tsien, M. Ormö and S. J. Remington, *Proc. Natl. Acad. Sci. U. S. A.*, 1997, **94**, 2306-2311.

6 A. D. Kummer, J. Wiehler, T. A. Schüttrigkeit, B. W. Berger, B. Steipe and M. E. Michel-Beyerle, *ChemBioChem*, 2002, **3**, 659-663.

7 C. Fang, R. R. Frontiera, R. Tran and R. A. Mathies, *Nature*, 2009, **462**, 200-204.

8 B. G. Oscar, W. Liu, Y. Zhao, L. Tang, Y. Wang, R. E. Campbell and C. Fang, *Proc. Natl. Acad. Sci. U. S. A.*, 2014, **111**, 10191-10196.

9 C. Fang, L. Tang, B. G. Oscar and C. Chen, *J. Phys. Chem. Lett.*, 2018, **9**, 3253–3263.

10 P. Kukura, D. W. McCamant and R. A. Mathies, *Annu. Rev. Phys. Chem.*, 2007, **58**, 461-488.

11 D. R. Dietze and R. A. Mathies, *ChemPhysChem*, 2016, **17**, 1224–1251.

12 J.-M. L. Pecourt, J. Peon and B. Kohler, *J. Am. Chem. Soc.*, 2001, **123**, 10370-10378.

13 E. T. J. Nibbering, H. Fidder and E. Pines, *Annu. Rev. Phys. Chem.*, 2005, **56**, 337-367.

14 R. M. Hochstrasser, *Proc. Natl. Acad. Sci. U. S. A.*, 2007, **104**, 14190-14196.

15 W. Liu, Y. Wang, L. Tang, B. G. Oscar, L. Zhu and C. Fang, *Chem. Sci.*, 2016, **7**, 5484-5494.

16 Y.-X. Yan, E. B. Gamble and K. A. Nelson, *J. Chem. Phys.*, 1985, **83**, 5391-5399.

17 D. P. Hoffman and R. A. Mathies, *Acc. Chem. Res.*, 2016, **49**, 616-625.

18 G. Batignani, G. Fumero, S. Mukamel and T. Scopigno, *Phys. Chem. Chem. Phys.*, 2015, **17**, 10454-10461.

19 B. G. Levine and T. J. Martínez, *Annu. Rev. Phys. Chem.*, 2007, **58**, 613-634.

20 J. P. Kraack, A. Wand, T. Buckup, M. Motzkus and S. Ruhman, *Phys. Chem. Chem. Phys.*, 2013, **15**, 14487-14501.

21 G. D. Scholes, G. R. Fleming, L. X. Chen, A. Aspuru-Guzik, A. Buchleitner, D. F. Coker, G. S. Engel, R. van Grondelle, A. Ishizaki, D. M. Jonas, J. S. Lundeen, J. K. McCusker, S. Mukamel, J. P. Ogilvie, A. Olaya-Castro, M. A. Ratner, F. C. Spano, K. B. Whaley and X. Zhu, *Nature*, 2017, **543**, 647-656.

22 C. Chen, W. Liu, M. S. Baranov, N. S. Baleeva, I. V. Yampolsky, L. Zhu, Y. Wang, A. Shamir, K. M. Solntsev and C. Fang, *J. Phys. Chem. Lett.*, 2017, **8**, 5921–5928.

23 C. Chen, M. S. Baranov, L. Zhu, N. S. Baleeva, A. Y. Smirnov, S. Zaitseva, I. V. Yampolsky, K. M. Solntsev and C. Fang, *Chem. Commun.*, 2019, **55**, 2537-2540.

24 C. Chen, L. Zhu, M. S. Baranov, L. Tang, N. S. Baleeva, A. Y. Smirnov, I. V. Yampolsky, K. M. Solntsev and C. Fang, *J. Phys. Chem. B*, 2019, DOI: 10.1021/acs.jpcb.1029b03201.

25 M. S. Baranov, K. A. Lukyanov, A. O. Borissova, J. Shamir, D. Kosenkov, L. V. Slipchenko, L. M. Tolbert, I. V. Yampolsky and K. M. Solntsev, *J. Am. Chem. Soc.*, 2012, **134**, 6025-6032.

26 S. S. Stavrov, K. M. Solntsev, L. M. Tolbert and D. Huppert, *J. Am. Chem. Soc.*, 2006, **128**, 1540-1546.

27 M. J. Frisch, G. W. Trucks, H. B. Schlegel, G. E. Scuseria, M. A. Robb, J. R. Cheeseman, G. Scalmani, V. Barone, B. Mennucci, G. A. Petersson, H. Nakatsuji, M. Caricato, X. Li, H. P. Hratchian, A. F. Izmaylov, J. Bloino, G. Zheng, J. L. Sonnenberg, M. Hada, M. Ehara, K.

Toyota, R. Fukuda, J. Hasegawa, M. Ishida, T. Nakajima, Y. Honda, O. Kitao, H. Nakai, T. Vreven, J. J. A. Montgomery, J. E. Peralta, F. Ogliaro, M. Bearpark, J. J. Heyd, E. Brothers, K. N. Kudin, V. N. Staroverov, R. Kobayashi, J. Normand, K. Raghavachari, A. Rendell, J. C. Burant, S. S. Iyengar, J. Tomasi, M. Cossi, N. Rega, J. M. Millam, M. Klene, J. E. Knox, J. B. Cross, V. Bakken, C. Adamo, J. Jaramillo, R. Gomperts, R. E. Stratmann, O. Yazyev, A. J. Austin, R. Cammi, C. Pomelli, J. W. Ochterski, R. L. Martin, K. Morokuma, V. G. Zakrzewski, G. A. Voth, P. Salvador, J. J. Dannenberg, S. Dapprich, A. D. Daniels, Ö. Farkas, J. B. Foresman, J. V. Ortiz, J. Cioslowski and D. J. Fox, *Gaussian 09, Revision B.1*, Gaussian, Inc., Wallingford, CT, 2009.

28 A. P. Esposito, P. Schellenberg, W. W. Parson and P. J. Reid, *J. Mol. Struct.*, 2001, **569**, 25-41.

29 J. P. Merrick, D. Moran and L. Radom, *J. Phys. Chem. A*, 2007, **111**, 11683-11700.

30 M.-A. Elsliger, R. M. Wachter, G. T. Hanson, K. Kallio and S. J. Remington, *Biochemistry*, 1999, **38**, 5296-5301.

31 A. F. Bell, X. He, R. M. Wachter and P. J. Tonge, *Biochemistry*, 2000, **39**, 4423-4431.

32 S. P. Laptenok, J. Conyard, P. C. B. Page, Y. Chan, M. You, S. R. Jaffrey and S. R. Meech, *Chem. Sci.*, 2016, **7**, 5747-5752.

33 G. Granucci, J. T. Hynes, P. Millie and T.-H. Tran-Thi, *J. Am. Chem. Soc.*, 2000, **122**, 12243-12253.

34 D. B. Spry, A. Goun and M. D. Fayer, *J. Phys. Chem. A*, 2007, **111**, 230-237.

35 D. B. Spry and M. D. Fayer, *J. Chem. Phys.*, 2008, **128**, 084508.

36 Y. Wang, L. Tang, W. Liu, Y. Zhao, B. G. Oscar, R. E. Campbell and C. Fang, *J. Phys. Chem. B*, 2015, **119**, 2204-2218.

37 T. Kumpulainen, B. Lang, A. Rosspeintner and E. Vauthey, *Chem. Rev.*, 2017, **117**, 10826-10939.

38 J. L. McHale, *Molecular Spectroscopy*, Prentice-Hall, Upper Saddle River, NJ, 1999.

39 X. He, A. F. Bell and P. J. Tonge, *FEBS Lett.*, 2003, **549**, 35-38.

40 A. Usman, O. F. Mohammed, E. T. J. Nibbering, J. Dong, K. M. Solntsev and L. M. Tolbert, *J. Am. Chem. Soc.*, 2005, **127**, 11214-11215.

41 D. Mandal, T. Tahara and S. R. Meech, *J. Phys. Chem. B*, 2004, **108**, 1102-1108.

42 M. E. Martin, F. Negri and M. Olivucci, *J. Am. Chem. Soc.*, 2004, **126**, 5452-5464.